Modelling the first droplet emission from an electrified liquid meniscus hanging at the nozzle tip

Hao Chen[1], Guozhen Wang[2], Tao An[1], Zhouping Yin[2] and Haisheng Fang[1],†

[1] School of Energy and Power Engineering, Huazhong University of Science and Technology, Wuhan, Hubei 430074, PR China

[2] State Key Laboratory of Intelligent Manufacturing Equipment and Technology, Huazhong University of Science and Technology, Wuhan, Hubei 430074, PR China

Electrohydrodynamic (EHD)-induced droplet emission is an efficient method for the production of micron- and submicron-sized droplets in technological applications. Existing studies propose several scaling laws to determine the size of the emitted droplet. However, they have usually focused on the tip streaming phenomena of a droplet when subjected to a uniform electric field. In most applications, a non-uniform distribution of the electric field is created owing to the nozzle-to-plate configuration. Here, we employ an arbitrary Lagrangian–Eulerian method to demonstrate the mechanism of the first droplet emission from an electrified liquid meniscus with a fixed volume hanging at the nozzle tip. The critical condition when tip streaming occurs is determined using our numerical results. A phase diagram in terms of the electric field and initial liquid volume is presented to obtain the commonly used jetting mode. The effects of the liquid volume, electric field strength and electrical conductivity of the liquid on the processes of jet formation and breakup are further investigated. We find a particularly non-monotonic dependence of the size of the emitted droplet on the electrical conductivity. These findings could be useful for generating microdroplets and improving injection frequency in EHD printing technology.

Key words: electrohydrodynamic effects, drops, breakup/coalescence

1. Introduction

When a liquid is subjected to a sufficiently strong electric field, it may deform and then emit charged droplets via the breakup of a preformed thin jet. The phenomenon of such jets into charged droplets has been widely used in a number of applications including

† Email address for correspondence: hafang@hust.edu.cn

electrospray (Fenn *et al.* 1989), electrospinning (Wendorff, Agarwal & Greiner 2012) and electrohydrodynamic (EHD) printing (Park *et al.* 2007). During the EHD printing process, a high electric potential is applied between the capillary nozzle and grounded collector, such that the meniscus of an ink liquid hanging at the nozzle tip will form a Taylor cone under the electric normal and tangential forces, and may produce mono-dispersed droplets. One practical advantage of EHD printing is that it allows for sub-micrometre resolution, which is typically beyond the capability of conventional piezoacoustic inkjet printing (Basaran, Gao & Bhat 2013; Lohse 2022) in which a typical droplet diameter is 20 μm. The emitted droplet in EHD printing is more than an order of magnitude smaller than the size of the nozzle. In the past few decades, EHD printing has been finding application in gradually increasing numbers of areas. Therefore, understanding this physical phenomenon is of utmost importance, as well as studying the mechanism of droplet emission.

In this study, we focus on the droplet emission from an electrified liquid meniscus hanging at the nozzle tip in which there is no liquid supply from the nozzle. Over a century ago, Zeleny (1917) experimentally reported the appearance of a liquid surface undergoing disintegration owing to an electric field. Subsequently, numerous efforts have been devoted to revealing this phenomenon. Taylor (1964) theoretically showed that a conical interface can be formed with a cone (i.e. Taylor cone) angle of 49.29° between two fluids subjected to an electric field. Melcher & Taylor (1969) first defined electrohydrodynamics as a branch of fluid mechanics with electric effects. After that, researchers have revealed remarkable phenomena concerned with the fluid motion in the presence of an electric field such as the tip streaming (i.e. cone jetting) from liquid cones. Past experimental studies have indicated that tip streaming is related to interfacial instability. The dynamics of jet breakup and drop formation are comprehensively discussed in previous works (Gañán-Calvo *et al.* 1994, 2016; López-Herrera, Herrada & Gañán-Calvo 2023). They developed theoretical models used to study the scaling laws of the size and the electric current of the droplets emitted from the liquid. They also focused on the electrospraying technique in the cone-jetting mode, including the complex charge relaxation and electrokinetic effect (López-Herrera *et al.* 2023). Collins *et al.* (2008) reported simulations and experiments to explain the mechanisms of cone formation and jet emission from a liquid film of finite conductivity. They showed that tip streaming cannot be observed if the liquid is perfectly conducting or insulating. The scaling regime for the size and charge of droplets was determined by their theory and simulation (Collins *et al.* 2013). Recently, Vlahovska (2019) reviewed the electrohydrodynamics of droplets and vesicles in electric fields. The symmetry-breaking of droplets was discussed due to the Quincke rotation effect, which is quite different from the tip streaming.

Tip streaming has been shown to be very advantageous in EHD printing, where the printed ink is continuously fed by a metallic nozzle. A constant voltage is applied between the conductive nozzle and the collector. Both printing modes and sizes of the emitted droplets are important for a high printing resolution in the fabrication process. Cloupeau & Prunet-Foch (1990, 1994) have reviewed the main functioning modes in EHD spraying, which can be classified from how the drops are emitted. When the voltage difference is low and the flow rate is sufficient, a droplet can be detached from the nozzle under the electric force; this is called the dripping mode. The single droplet has a diameter similar to that of the capillary nozzle. The formation of droplets from capillary tubes in the presence of an electric field has been analysed by Notz & Basaran (1999). They classified different regimes as a function of the electric field and gravitational force. When the electric field is high enough, a long liquid jet will be emitted from the meniscus hanging from the nozzle tip and further break up into multiple microdroplets under the Plateau–Rayleigh

instability; this is called the jetting mode. The transition from dripping to EHD jetting has been studied experimentally and numerically by previous researchers. Lee *et al.* (2013) systemized six dimensionless numbers to draw a jetting map for an EHD printing system. A stable cone jet can be obtained by optimizing the experimental parameters. Guan *et al.* (2022) numerically studied high-frequency pulsating EHD jet printing and explained the impacts of voltage on the different printing stages. Additionally, Hijano, Loscertales & Higuera (2021) suggested that there is a periodic micro-dripping mode apart from the typical dripping and jetting modes. In this mode, a ligament is detached from the electrified meniscus and further disintegrates into one or several monodispersed droplets. Beyond these three modes, extensive studies have been devoted to revealing the other jetting modes such as the tilted-jet, twin-jet, multi-jet and spindle modes (Lee *et al.* 2013; Verdoold *et al.* 2014; Gañán-Calvo *et al.* 2018; Montanero & Gañán-Calvo 2020; Kong *et al.* 2022).

In EHD printing, it would be preferable if the printing mode is steady and the emitted droplets are in the right range of sizes. There are two main problems: the stability of tip streaming and the breakup of liquid jet. The jet initiation can be affected by many parameters, including the physical properties of the liquid, the applied electric field, the geometry of the system and the flow rate (Cisquella-Serra *et al.* 2019; Gamero-Castaño & Magnani, 2019; Gallud & Lozano, 2022). Harris & Basaran (1993) determined the equilibrium shapes and stability of a conducting drop hanging from a nozzle. In their study, they discussed the effect of the nozzle on the equilibrium shapes of pendant drops with fixed volume. Beroz, Hart & Bush (2019) determined the stability limit of a droplet subjected to a uniform electric field. They found a single power law between the droplet volume and electric field to predict the critical condition for tip streaming. Rubio *et al.* (2021) studied the onset of tip streaming in an electrified droplet and pointed out the role of charge relaxation during the jetting process. In particular, they experimentally determined the charge of the first-emitted droplet in the cone-jet mode. Despite this, previous studies have usually focused on the pendant droplet subjected to a uniform electric field, which is created by plate-to-plate electrodes (i.e. parallel electrodes), while for EHD printing in a steady cone-jet mode, a nozzle-to-plate configuration is often used for an intense electric field. The characteristic electric field strength at the nozzle tip can be calculated as $E = 2\hat{\phi}/[R_0 \ln(4H/R_0)]$, where $\hat{\phi}$ is the potential difference between the two electrodes, R_0 is the nozzle radius, and H is the distance between the nozzle tip and the counter electrode (Marginean, Nemes & Vertes 2006). The critical condition for the occurrence of tip streaming has not been determined for this case, namely, that of a liquid meniscus (or pendant droplet) hanging at the nozzle tip subjected to a needle-to-plate electric field.

In this work, we focus on the mechanism of tip streaming using a numerical method. The difficulty in modelling this phenomenon arises from the charge transport along the liquid–air interface. In previous numerical studies, the liquid is usually treated as a Taylor–Melcher leaky dielectric, where the charge is zero in the bulk and charge relaxation only occurs at the liquid interface (Saville 1997). The surface charge density satisfies the conservation equation including the flow-induced charge convection and Ohmic conduction caused by the movement of free electrons. Using the leaky dielectric model, the electrohydrodynamic tip streaming has been numerically simulated using distinct approaches such as the volume of fluid (VOF) method (Gawande, Mayya & Thaokar 2019), level set (LS) method (Nie et al. 2021*a*), phase field (PF) method (Zhong *et al.* 2023), boundary element method (BEM) (Gamero-Castaño & Magnani 2018; Hijano *et al.* 2021) and arbitrary Lagrangian–Eulerian (ALE) algorithm (Wagoner *et al.* 2021). Here we employed the ALE algorithm to model the jet emission and breakup that occur during the tip streaming. This is similar to the work developed by Collins *et al.* (2008, 2013),

except that now the electric field is created by the nozzle electrode and collector electrode. This sharp interface method (Anthony *et al.* 2023) has been used extensively to model EHD problems since it allows a complete formulation of the charge conservation across the interface. In this paper, we focus on the nozzle-to-plate configuration, where a liquid meniscus is hanging at the nozzle tip with no liquid supply. The critical condition when tip streaming occurs is determined using our numerical results. We then exhibit a simple phase diagram delineating the non-jetting to jetting transition in terms of the electric field and initial liquid volume. Finally, the effects of fundamental variables, namely the liquid volume, the electric field strength and the electrical conductivity of liquid on the processes of jet formation and breakup are further investigated.

2. Problem formulation

Figure 1(*a*) shows the sketch of the two-dimensional axisymmetric computational domain used in our simulation. A liquid meniscus of density ρ_l, viscosity μ_l, electrical permittivity ε_l and electrical conductivity σ_l hangs from a metallic nozzle of length R_0, inner radius aR_0 and outer radius bR_0, where $a \leq 1$ and $b \geq 1$. In this study, the meniscus is numerically pinned to the nozzle tip at a fixed contact radius R_0; therefore, $a = 1$ and $b = 1$ represent that the meniscus is pinned to the sharp edge of the inner and outer nozzle wall, respectively. To avoid the numerical difficulty in modelling the two limiting cases, we choose $a = 0.9$ and $b = 1.1$, indicating that the contact line is pinned to the middle of the nozzle tip. For the initial condition ($t = 0$), a static liquid meniscus of volume $\mathcal{V} = \pi R_0^3 (1 - \cos\theta_0)^2 (2 + \cos\theta_0)/3\sin^3\theta_0$ hangs from the nozzle tip. Here, θ_0 represents both the contact angle and the opening half-angle of the meniscus shape. Likewise, the liquid meniscus is surrounded by the air of density ρ_a, viscosity μ_a, electrical conductivity σ_a and electrical permittivity ε_a equal to that of vacuum $\varepsilon_0 = 8.85 \times 10^{-12}$ F m^{-1}. The surface tension γ of the liquid–air interface and the physical properties of the two fluids are taken to be constant and uniform.

Two-phase Navier–Stokes equations are solved for the two fluids in a cylindrical region (r, z) with a radius of W and a height of $H + L$; see figure 1(*a*). Here, r and z stand for the radial and axial coordinates, respectively. The electric field is created by applying different electric potentials ϕ on the metallic nozzle ($\phi = \phi_0$) and the circular collector ($\phi = 0$). Thus, the electric field points from the nozzle to the collector. The length of the nozzle and its distance to the collector are taken to be L and H, respectively. We note that in actual experiments, the length of the nozzle and the radius of the collector are always much larger than the radius of the nozzle, e.g. $L = 20$ mm, $W = 31.5$ mm and $R_0 = 0.25$ mm in the experiments of Hijano *et al.* (2015). To save calculation time, we use the infinite element domain in which the physical domain is surrounded by a layer of virtual domain that extends to infinity, as shown in figure 1(*a*). In this way, the nozzle and collector are assumed to have a large physical dimension, which subsequently affects the solution. It is noted that the infinite element domain is only used to solve the electric field. In this study, we set $W = 10R_0$, $L = R_0$ and $H = 20R_0$. We have checked the results and verified that the electric field is hardly affected by increasing the size of the computational domain in this case.

In what follows, it is convenient to show the equations in dimensionless form. The problem can be dimensionalized using the characteristic length scale $l_c = R_0$, capillary time scale $t_c = \sqrt{\rho_l R_0^3/\gamma}$, stress scale $p_c = \gamma/R_0$, electric field strength scale $E_c = E_0 = 2\hat{\phi}/[R_0 \ln(4H/R_0)]$ and surface charge density scale $q_c = \varepsilon_0 E_0$. It is noted that all variables will be made dimensionless in the following discussion unless stated otherwise.
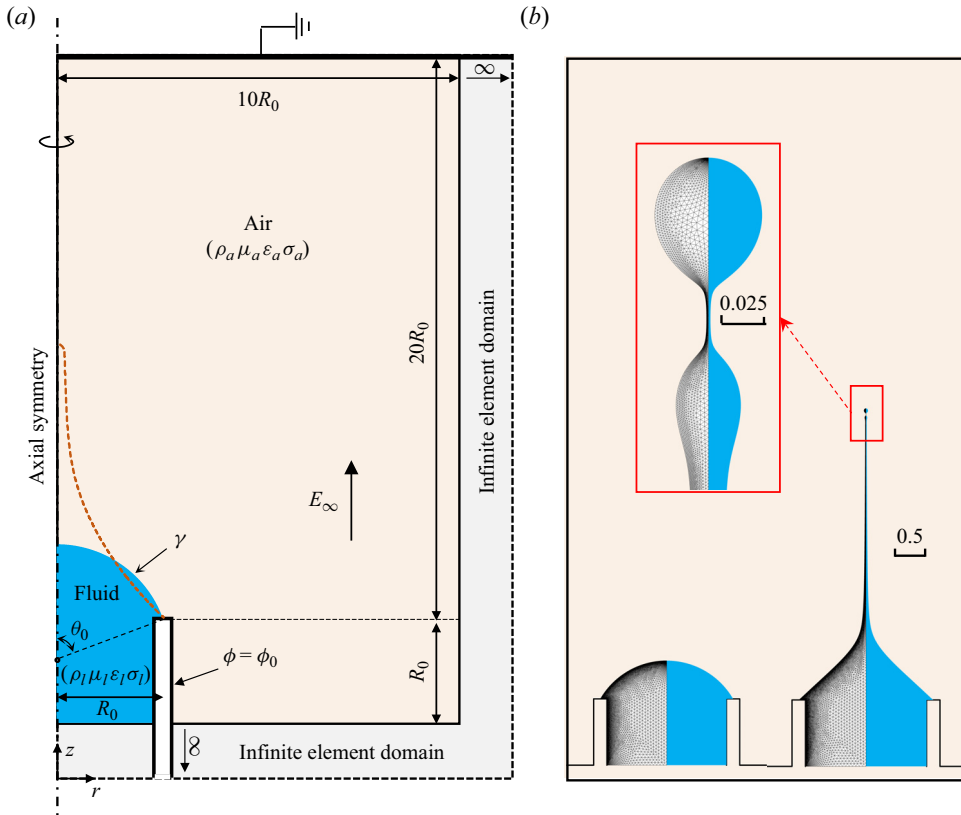
Figure 1. (*a*) Sketch of the numerical model considered in this work. (*b*) Initial condition (left) of the system and the simulated emission (right) of a charged drop from the meniscus at the onset of pinch-off. The zoomed-in view shows the jet's tip and the mesh refinement. Here, $\theta_0 = 60°$ for the initial condition.

The incompressible Navier–Stokes equations for the velocity $\boldsymbol{u}$ and pressure p inside the liquid domain (Ω_l) are

$$\boldsymbol{\nabla} \cdot \boldsymbol{u} = 0 \quad \text{in } \Omega_l, \tag{2.1}$$

$$\frac{\partial \boldsymbol{u}}{\partial t} + \boldsymbol{u} \cdot \boldsymbol{\nabla} \boldsymbol{u} = -\boldsymbol{\nabla} p + Oh \nabla^2 \boldsymbol{u} + Bo\boldsymbol{i}_z \quad \text{in } \Omega_l. \tag{2.2}$$

Here, $Oh = \mu_l / \sqrt{\rho_l R_0 \gamma}$ is the dimensionless Ohnesorge number, $Bo = \rho_l g R_0^2 / \gamma$ is the Bond number, g is the gravity acceleration and $\boldsymbol{i}_z$ is the unit vector in the direction of g. The electric potential ϕ satisfies the Laplace's equation in both phases:

$$\nabla^2 \phi = 0 \quad \text{in } \Omega_l \text{ and } \Omega_a, \tag{2.3}$$

and thus the electric field is expressed as $\boldsymbol{E} = -\boldsymbol{\nabla} \phi$.

Along the liquid–gas interface S_f, the Maxwell stresses are added into the traction condition so that the flow and electric field are coupled. The stress balance is expressed as

$$\boldsymbol{n} \cdot [\boldsymbol{T}_i^H + \boldsymbol{T}_i^E]_l^g = \kappa \boldsymbol{n} \quad \text{on } S_f, \tag{2.4}$$

where

$$\boldsymbol{T}_i^H = -p_i \boldsymbol{I} + Oh_i(\boldsymbol{\nabla} \boldsymbol{u} + (\boldsymbol{\nabla} \boldsymbol{u})^{\mathrm{T}}) \tag{2.5}$$

987 A38-5

and

$$T_i^E = Ca_E \varepsilon_i (EE - E^2 I/2) \qquad (2.6)$$

are the hydrodynamic stress tensor and the Maxwell stress tensor, respectively. On the left-hand side of (2.4), $[x_i]_l^g$ denotes the jump in a quantity x in going from phase l to phase g; l and g represent the quantity on the liquid and gas sides of S_f, respectively; $\boldsymbol{n}$ is the unit vector normal to the interface pointing away from the liquid and $\kappa = \nabla \cdot \boldsymbol{n}$ is twice the mean curvature of the interface. The electric capillary number $Ca_E = \varepsilon_0 E_0^2 R_0/\gamma$ is used to measure the ratio of electric to capillary force. Also along the liquid–gas interface, the surface charge density q is given by the Gauss law, $q = \boldsymbol{n} \cdot [\varepsilon_i \boldsymbol{E}_i]_l^g$, which represents the normal jump in the electric displacement. For the leaky-dielectric model, the bulk density of charge is zero but the surface charge density q obeys the charge transport equation

$$\frac{\partial q}{\partial t} + \nabla_s \cdot (q\boldsymbol{u}) - \frac{1}{Pe}\nabla_s^2 q = \frac{\varepsilon_l}{\varepsilon_g}\alpha\boldsymbol{n} \cdot \left[\boldsymbol{E}_l - \frac{\sigma_g}{\sigma_l}\boldsymbol{E}_g\right] \quad \text{on } S_f, \qquad (2.7)$$

where $\nabla_s = (\boldsymbol{I} - \boldsymbol{nn}) \cdot \nabla$ is the surface gradient. The left-hand side of (2.7) shows the accumulation, convection and diffusion of the surface charge, respectively. The Péclet number $Pe = R_0^2/D_c t_c$ denotes the ratio of the time scale R_0^2/D_c for charge diffusion and the capillary time t_c, where D_c is the surface diffusion coefficient. On the right-hand side of (2.7), $\alpha = t_c/t_e = \sqrt{\rho_l R_0^3 \sigma_l^2/\gamma \varepsilon_l^2}$ is the dimensionless charge relaxation parameter, where $t_e = \varepsilon_l/\sigma_l$ is the charge relaxation time. This source-like term represents the charge transport by Ohmic conduction. In the limit that the surface charge transport is dominated by Ohmic conduction ($\alpha \to \infty$ or $\sigma_l \to \infty$), the fluid behaves as a perfect conductor. To prohibit the mass transfer across the interface, the kinematic boundary condition is applied along S_f,

$$\boldsymbol{n} \cdot (\boldsymbol{u} - \boldsymbol{u}_s) = 0 \quad \text{on } S_f, \qquad (2.8)$$

where $\boldsymbol{u}_s$ is the velocity of points on S_f. Dirichlet boundary conditions on ϕ are imposed on the nozzle ($\phi = \phi_0$), the grounded collector ($\phi = 0$) and the corresponding parts in the infinite element domain. In the present study, $\phi_0 = \ln(80)/2$, calculated from the physical position of nozzle and collector. Neumann boundary conditions $\boldsymbol{n} \cdot \boldsymbol{E} = 0$ are imposed on the right and bottom boundaries. Symmetry conditions are set along the symmetry axis ($r = 0$) for the solution of flow and electric field. No-slip and no-penetration conditions on $\boldsymbol{u}$ are imposed along the nozzle wall.

In our study, we focus on the influence of three parameters, the opening half-angle θ_0 (i.e. the initial volume of the meniscus), the electric capillary number Ca_E (i.e. the electric field strength) and the charge relaxation parameter α (i.e. the electrical conductivity), on the emission process of charged drops from a nozzle. Here we set $Oh = 0.1$ since it stands for easy observation of the interplay between the viscous, inertial and electric forces. The effect of gravity is ignored because the Bond number $Bo \ll 1$ in most applications. Table 1 summarizes the values of the other constant parameters used in the current study.

3. Numerical scheme and validation

Equations (2.1)–(2.8) are numerically solved via the ALE algorithm, in which the computational mesh can move to deform the interface. To this end, we employed the finite-element software COMSOL Multiphysics. The built-in package enables us to model

Viscosity ratio, μ_l/μ_g	Density ratio, ρ_l/ρ_g	Conductivity ratio, σ_l/σ_g	Permittivity ratio, $\varepsilon_l/\varepsilon_g$	Péclet number, Pe
269	1000	1×10^6	10	1000

Table 1. Properties of the fluids.

the two-phase interface and couple the electric field and shear-induced deformation. In the underlying problem, triangular elements were adopted in the computational domain. Moreover, we note that the treatment of droplet emission from the apex of the liquid–air interface must require special attention. The minimum size of the mesh is determined by the radius R_d of the droplet formed from EHD tip streaming. Here we use a coordinate-dependent function to specify the size of mesh elements evaluated on the liquid–air interface. An example mesh is shown in figure 1(*b*). The local mesh size h on the interface is a square root function of the radial coordinates r of the points. The minimum size is $h_{min} = 2 \times 10^{-5}$ at $r = 0$ and the maximum size is $h_{max} = 5 \times 10^{-3}$ at $r = 1$. Moreover, 0.05 and 0.25 are used as a limit of the maximum size for the infinite element domain and the fluid domain, respectively. However, the quality of moving mesh becomes worse as the tip streaming occurs so that an automatic remeshing technique is adopted to remesh the deformed domain. When the mesh quality becomes less than a given limit, the software will automatically remesh the computational domain using the specified function of mesh size and immediately reinitialize the solution. A typical snapshot of the remeshed sequence is shown in the zoomed-in region in figure 1(*b*). A particular advantage of this method is that we can model the emission of a very tiny droplet, e.g. $R_d/R_0 < 0.001$; see the results in § 4.3. Time integration is handled with a backwards differentiation formula (BDF) with an adaptive time step and specified time step constraint. The system is solved by a multifrontal massively parallel sparse direct solver (MUMPS) coupled with a constant Newton's method. Further details on the numerical scheme can be found in our previous study (Chen et al. 2023).

We then present the validation of our numerical model used to analyse the problem. In figure 2, the simulated result is compared with the reported experimental study of Ferrera *et al.* (2013). In their experiments, two parallel circular electrodes of radius $W = 5$ cm and $H = 10$ cm were used to create a uniform electric field. Initially, a static drop of volume $\mathcal{V} = 3.26R_0^3$ (i.e. $\theta_0 = 105.6°$) hung from an orifice surrounded by air with a contact radius $R_0 = 2$ mm. The working liquid was 1-octanol with $\mu_l/\mu_g = 478$, $\rho_l/\rho_g = 824$, $\sigma_l/\sigma_g = 9 \times 10^5$ and $\varepsilon_l/\varepsilon_g = 10.3$. From their given data, the dimensionless parameters are calculated as $Oh = 0.0431$, $Ca_E = 0.11$, $Bo = 1.27$ and $\alpha = 157.5$. Figure 2 shows the droplet shapes at different times in the simulation and experiment. A tip streaming appears in the droplet apex, followed by the breakup of the charged jet into a tiny droplet of radius $R_d = 10.1$ µm. It is confirmed that our numerical model can well reproduce the experimental sequence. Moreover, the Taylor cone and emitted droplet formed at the droplet tip are clearly observed in the last two images. This means that the numerical method can capture the tip streaming beyond the limitation of high-speed imaging. Moreover, the charge relaxation in our electrohydrodynamic model is validated by simulating the deformation of a droplet when subjected to an electric field. Please refer to Appendix A for details.
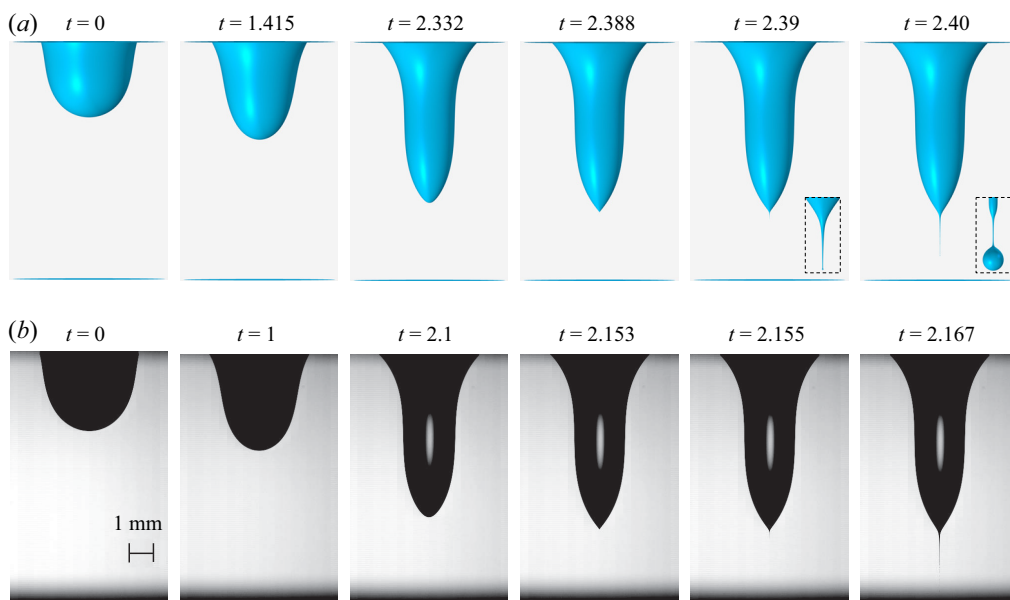
Figure 2. Side-view snapshots of an electrified pendant droplet during the tip streaming process at different dimensionless times for $\theta_0 = 105.6°$, $Oh = 0.0431$, $Ca_E = 0.11$, $Bo = 1.27$ and $\alpha = 157.5$. Here the electric field is created by two parallel electrodes. The insets in the last two images show the magnified view of the jet's tip. Reprinted with permission from Ferrera *et al.* (2013). Copyright 2013 AIP Publishing.

4. Results and discussion

4.1. *Critical condition for tip streaming*

We begin our study by presenting the stability limit, i.e. the critical condition when tip streaming occurs, of a liquid meniscus in the general case. Figure 3(*a*) shows the phase diagram as a function of the dimensionless electric capillary number Ca_E and the opening half-angle θ_0 at fixed charge relaxation parameter $\alpha = 10$. It is noted that the critical condition is expected to be independent of the liquid properties, except the surface tension (Rubio *et al.* 2023). Three distinct regimes are observed: jetting, non-jetting and dripping. Figure 3(*b*) shows the meniscus shapes in these three regimes at the instants when pinch-off occurs or the meniscus becomes stable. In the non-jetting regime, for example, $\theta_0 = 90°$ and $Ca_E = 1.31$, the meniscus will oscillate under the electric and capillary forces. Then the oscillation is damped out due to the viscous effect and the meniscus eventually approaches a stable state. However, when the electric field is slightly improved, $Ca_E \rightarrow 1.32$, the shape of the meniscus tip becomes a Taylor cone. The tip streaming subsequently appears in the meniscus apex, resulting in a continuously growing jet, which is called the jetting regime. It is noted that the jetting regime is defined as the cases with the occurrence of a tip-streaming jet in our study. The radius of the jet is two orders of magnitude smaller than the nozzle radius. Figure 3(*a*) demonstrates that the increase in θ_0 remarkably decreases the critical electric capillary number $Ca_{E,c}$ required for jetting. This is because the variation of surface energy of the meniscus and electrostatic energy of the electric field are both affected by increasing the opening half-angle θ_0, namely, increasing the liquid volume. This reason is discussed in more detail below. When θ_0 is increased to be larger than $134°$, the meniscus undergoes a transition from non-jetting to dripping and jetting rather than non-jetting to jetting for $\theta_0 \leq 134°$. In this transitional
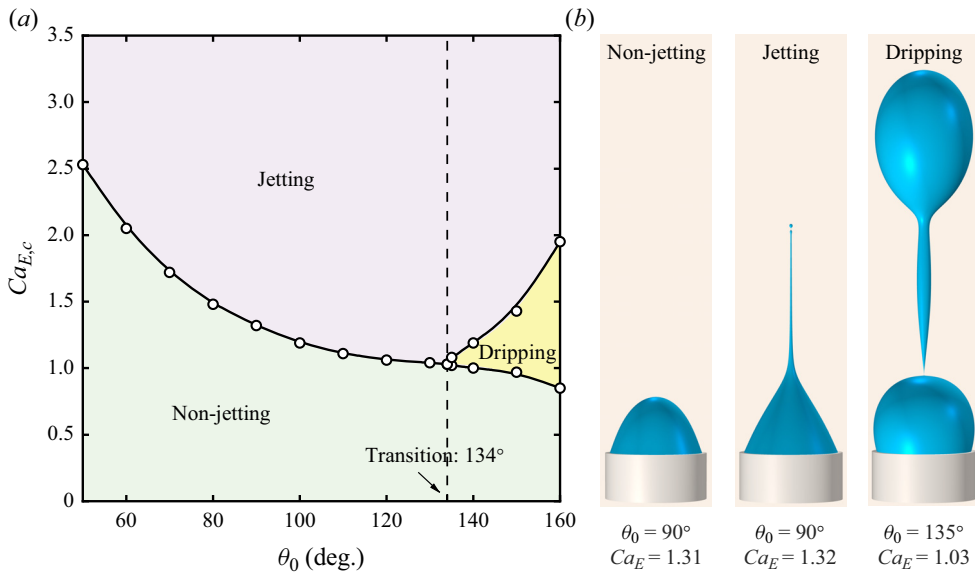
987 A38-8

Figure 3. (*a*) $Ca_E - \theta_0$ phase diagram indicating the jetting, non-jetting and dripping regimes. Here, $\alpha = 10$ and the data points represent the transitions between different regimes. The dashed line marks the case of $\theta_0 = 134°$. (*b*) Typical cases in these three regimes.

regime, the system will first enter a dripping regime. Figure 3(*b*) shows a typical case of the dripping regime, in which the size of the emitted droplet is of the same order of magnitude as the nozzle radius. Only when the electric field is increased further, the jetting can be obtained. Consequently, the critical number $Ca_{E,c}$ for jetting increases with increasing θ_0 for $\theta_0 > 134°$. In contrast, the critical number $Ca_{E,c}$ for dripping is decreased with increasing θ_0. The transition between these regimes can be understood from the crucial condition for the jetting behaviour: the electric field is high enough to generate a cone jet at the meniscus tip, as well as the requirement that the primary liquid does not detach from the nozzle. To satisfy the latter, the initial volume of the meniscus could not exceed a critical limit, i.e. $\theta_0 \leq 134°$; otherwise, the dripping would occur before jetting.

From figure 3(*a*), it is noted that neither jetting nor dripping is observed for $\theta_0 < 50°$. This is due to the non-uniform distribution of the electric field in the nozzle-to-plate configuration. For $\theta_0 < 50°$, when the electric field is continuously increased, the accumulated charge reaches the limit and a conical meniscus will first form near the nozzle rather than at the meniscus tip, which gives rise to the formation of multiple jets (Jaworek & Krupa 1999). This regime is not accounted for in the present study.

In figure 4, we recover the limiting cases of the jetting regime for different θ_0 in figure 3(*a*). Snapshots for each column respectively display the initial and final states of the meniscus at the incipience that the first droplet is emitted. As the liquid volume increases, the shape of each meniscus and its axial length differ drastically from each other, which is determined by the original liquid volume. The shapes of the liquid meniscus for different θ_0 have been experimentally reported in the literature (Verdoold *et al.* 2014; Kong *et al.* 2022). It is seen that the shapes of the transition region that connects the tip streaming jet and the Taylor cone are similar for all the limiting cases. However, when $\theta_0 \geq 134°$, the meniscus eventually takes on a spindle-like shape with a conical end at the incipience of pinch-off. A tiny droplet is then emitted from the spindle tip. From figure 4, it is clearly seen that the radius of the neck connecting the conical meniscus and the spindle
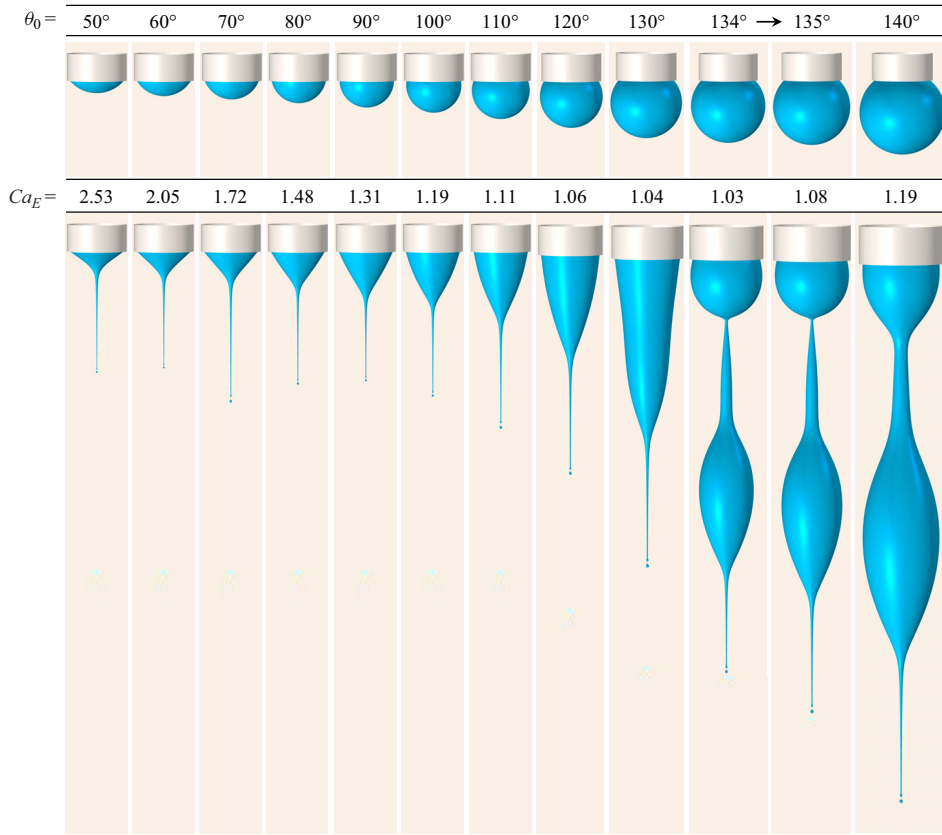
Figure 4. Simulated meniscus shapes for different θ_0 and $Ca_{E,c}$ in the limiting case of the jetting regime. Here, $\alpha = 10$. The upper images show the initial meniscus shapes and the lower images show the emission of the tip-streaming jet and the about-to-form droplet at the incipience of pinch-off.

is very small. The elongated jet resembling a spindle will certainly detach from the liquid meniscus and eventually form one or more satellite droplets. This jetting-before-dripping mode has been reported in the review of Cloupeau & Prunet-Foch (1994). However, in our study, we focus on the limiting cases when tip streaming occurs so that we prefer to treat this case as the jetting mode since the tip streaming has occurred before dripping. As θ_0 continues to increase, the size of the spindle is significantly increased, but the neck radius is slightly increased. We thereby conclude that for the single cone jetting, the initial liquid volume cannot exceed a critical value.

To qualitatively discuss the limiting cases, we plot in figure 5 the effect of θ_0 on the key parameters of the tip streaming processes. Figure 5(a) shows the variation of the pinch-off time t_p for different θ_0. It might be surprising that the pinch-off of the electrified jet occurs earlier ($t_p \approx 3$) for θ_0 ranging from $60°$ to $90°$. The pinch-off time will slightly increase when θ_0 decreases to $50°$. However, t_p is significantly increased with increasing θ_0 for $\theta_0 \geq 90°$. The maximum pinch-off time is found to be $t_p \approx 20$ for $\theta_0 = 134°$, which is exactly the critical limit for the transition regime. When θ_0 exceeds this critical limit, t_p will decrease again. This is primarily because the time scale for the dripping regime is larger than that for the jetting regime. The pinch-off time is therefore observed to reach its maximum near the transitional regime.
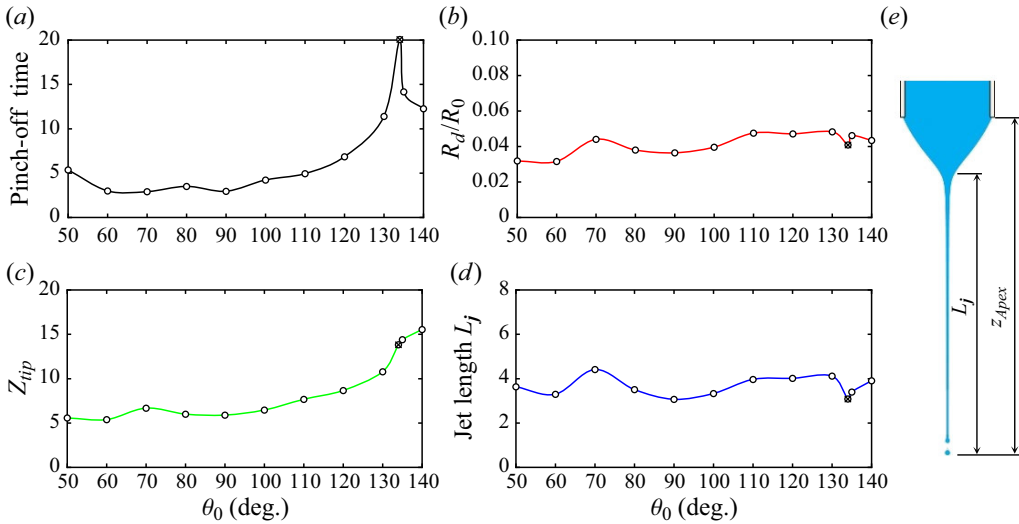
Figure 5. Effect of θ_0 on the meniscus shapes at the incipience of pinch-off in the limiting case of jetting. (*a*) Pinch-off time, (*b*) size of the first emitted droplet, (*c*) axial location of the jet's tip and (*d*) redefined length of the jet. Here, $\alpha = 10$ for all cases and the filled symbol represents the critical case of $\theta_0 = 134°$. (*e*) Definition of the jet length L_j.

As seen in figure 5(*b*), the size ratio R_d/R_0 is found to be approximately 0.04 for all limiting cases, indicating that θ_0 has little effect on the radius R_d of the emitted droplet. Here, R_d is calculated from $(3 \int_{z_{neck}}^{z_{tip}} \pi r^2 \, dz/4\pi)^{1/3}$, where z_{neck} is the axial coordinate of the neck point. Figure 5(*c*) shows the axial location of the jet's tip as a function of the opening half-angle. As one may expect, an increase in θ_0 leads to a longer jet. However, the axial location of the tip cannot reflect the jet's length because the initial values are distinct. The initial meniscus height is determined by the opening half-angle: $z_0 = R_0(1 - \cos\theta_0)/\sin\theta_0$. In this case, we redefine the jet length L_b as measured from the point where the change of the jet radius starts to be very small (Ismail *et al.* 2018). The definition of L_j is illustrated in figure 5(*e*), where the chosen point satisfies $\Delta r/\Delta z = 0.2$. In figure 5(*d*), it is surprising that the value of the redefined jet length is all around 4 and also has little dependence on θ_0. These results suggest that θ_0 has an effect only on the pinch-off time.

We proceed by theoretically demonstrating the correlation between the critical electric capillary number $Ca_{E,c}$ and the opening half-angle θ_0. For a sessile droplet subjected to a uniform electric field created by two parallel electrodes, Beroz *et al.* (2019) suggested that the critically stable droplet shapes correspond to the minima of the free energy, i.e. $dF = 0$. The free energy F consists of the surface energy $F_s = \gamma R_0^2 a(\xi)$ and electrostatic energy $F_E = \varepsilon_0 E_0^2 \mathcal{V} v(\xi)$. Here, $a(\xi)$ and $v(\xi)$ are the dimensionless shape functions. Thus, the differential $dF = 0$ becomes $\gamma R_0^2 a'(\xi) + \varepsilon_0 E_0^2 \mathcal{V} v'(\xi) = 0$, or equivalently, $a'(\xi)/v'(\xi) + (\varepsilon_0 E_0^2 R_0/\gamma)(\mathcal{V}/R_0^3) = 0$. For the critically stable shape, they infer that $a'(\xi)/v'(\xi)$ is a constant and the formula becomes

$$\frac{R_0^3}{\mathcal{V}} = kCa_E, \tag{4.1}$$

where the prefactor k is found to be $\pi/2$ from their experimental results. This simple scaling law yields the qualitative relation between the critical electric capillary number
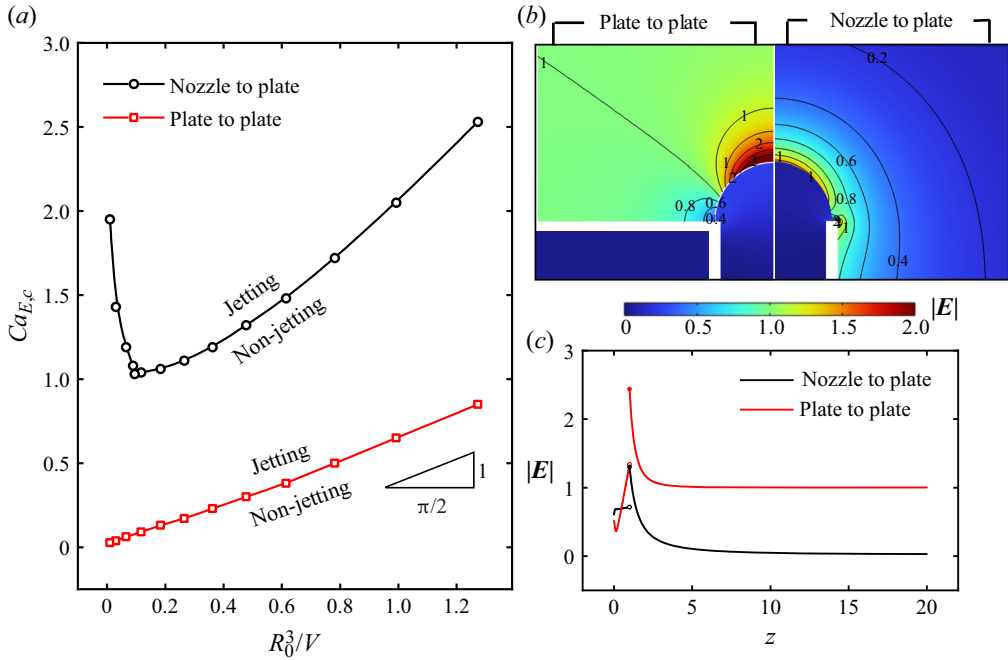
987 A38-11

Figure 6. (*a*) Critical electric capillary number $Ca_{E,c}$ as a function of the dimensionless shape function $R_0^3/\mathcal{V}$. A linear relationship is identified for the plate-to-plate configuration as reported by Beroz *et al.* (2019). (*b*) Distribution of electric field strength $|\boldsymbol{E}|$ inside and outside the droplet for the plate-to-plate configuration (left) and the meniscus for the nozzle-to-plate configuration (right). Here, $\theta_0 = 90°$ and $\alpha = 10$. The white regions represent the nozzle and plate. (*c*) Electric field strength along the interface and the symmetry axis as a function of the axial coordinate. Here, $z = 0$ denotes the triple contact point.

$Ca_{E,c}$ and the opening half-angle θ_0, because

$$\frac{R_0^3}{\mathcal{V}} = \frac{3\sin^3\theta_0}{\pi(1-\cos\theta_0)^2(2+\cos\theta_0)}. \tag{4.2}$$

We then replot $Ca_{E,c}$ as a function of $R_0^3/\mathcal{V}$, as shown in figure 6(*a*). Additionally, the plate-to-plate configuration has also been simulated using our numerical model with the same parameters. A horizontal electrode is included to create a uniform electric field. Figure 6(*b*) shows the distribution of electric field strength $|\boldsymbol{E}|$ inside and outside the droplet (or meniscus) for the plate-to-plate configuration and nozzle-to-plate configuration.

The red data points in figure 6(*a*) show a linear relationship between $Ca_{E,c}$ and $R_0^3/\mathcal{V}$ with a fitting constant $k = \pi/2$ for the plate-to-plate configuration. There is an excellent agreement between the prediction of (4.2) and our numerical results. It is noted that no dripping is observed among these cases, even for $\theta_0 \gg 134°$. However, for the nozzle-to-plate configuration, which is the one considered in this work, the critical value $Ca_{E,c}$ appears to be larger. The qualitative relation between $Ca_{E,c}$ and $R_0^3/\mathcal{V}$ for our considered model is quite different from that obtained in the theoretical study of Beroz *et al.* (2019). To this end, we look at the spatial distribution of the electric field in these two cases. Both the contour in figure 6(*b*) and spatial variation in figure 6(*c*) indicate that the electric field around the interface for the nozzle-to-plate configuration is smaller than that for the plate-to-plate configuration. This is because the characteristic electric field is

chosen to be the value at the nozzle tip for the nozzle-to-plate configuration rather than the uniform far field for the plate-to-plate configuration. This special geometry causes the local electric field to get weaker quickly with the axial distance, as shown in figure 6(*c*). Since the electric stress $T_i^E = Ca_E \varepsilon_i(\boldsymbol{EE} - E^2 \boldsymbol{I}/2)$ is determined by the electric fields on the two sides of the interface, a higher value is required for the critical electric capillary number $Ca_{E,c}$. However, it is noted that a higher $Ca_{E,c}$ does not indicate a higher electric potential applied on the nozzle because the definitions of characteristic electric field strength are different for the nozzle-to-plate and plate-to-plate configurations. The former is $E_0 = 2\hat{\phi}/[R_0 \ln(4H/R_0)]$ and the latter is $E_0 = \hat{\phi}/H$. For example, when $\theta_0 = 90°$, the critical electric potential difference is calculated as 1374 V for the nozzle-to-plate configuration but 5981 V for the plate-to-plate configuration; this is the reason why the nozzle-to-plate configuration is preferred in most applications.

Next, we turn our attention towards the transition of non-jetting, dripping and jetting regimes. The transitional opening half-angle is found to be 135°. We therefore plot in figure 7 the temporal dynamics in these three regimes with $Ca_E = 1.02$, 1.03 and 1.08, and $\theta_0 = 135°$. Figure 7(*a*) shows the simulated images of the meniscus shapes. Given almost the same Ca_E, the sequence exhibits an entirely different outcome. For $Ca_E = 1.02$, the electrified meniscus eventually reaches a stable state after an axial oscillation. However, when Ca_E is slightly increased to 1.03, dripping occurs. Under the electric field, the meniscus is stretched into a nearly cylindrical liquid that is attached to the capillary at $t = 12$. Then a neck begins to form and continues to thin. The neck quickly narrows down until the drop pinches off. Figure 7(*a*) shows that tip-streaming can only be observed until Ca_E is increased to 1.08. Among this range of Ca_E that dripping occurs, we find the radius R_d/R_0 of the emitted droplet is approximately 1.17. It is therefore concluded that this value determines the minimum size of droplets that can be produced by the dripping regime.

Figure 7(*b*–*d*) respectively show the temporal evolutions of the axial location, the charge density and the curvature at the tip for a meniscus deforming via different regimes. During the initial stage, the meniscus height in the jetting regime increases faster than that in the dripping regime. At $t = 13.85$, it rapidly increases from 9.64 to 13.36 during a very short period of $\Delta t = 0.3$. This is because the charge density has reached a limit value at this instant, which gives rise to a strong electrostatic force at the tip of the meniscus. The variations of the charge density and curvature further confirm this significant increase in the normal electric stress at the tip of the meniscus. We note that the charge density and the tip curvature simultaneously rise to values almost an order of magnitude higher than that in the dripping or non-jetting regimes. When tip streaming occurs, both the charge and curvature begin to decrease, suggesting that the charged droplet starts to be emitted from the jet's tip. It is noted that the charge density and the curvature are interdependent during the entire process, as shown in figure 7(*c*,*d*). From the results above, we can conclude that the key factor that determines the difference between these three regimes is the speed at which the tip charge density rises. To obtain the jetting regime, the surface charge must accumulate quickly enough at the meniscus tip so that the Taylor cone can form prior to dripping.

4.2. *Influence of opening half-angle on the tip streaming*

After discussing the critical condition for tip streaming by considering the limiting cases in the previous section, we will now elucidate the influences of three key parameters on the first emission of a charged droplet. Figure 8(*a*,*b*) shows the influence of the opening half-angle θ_0, i.e. the initial volume, on the meniscus shapes during the tip streaming
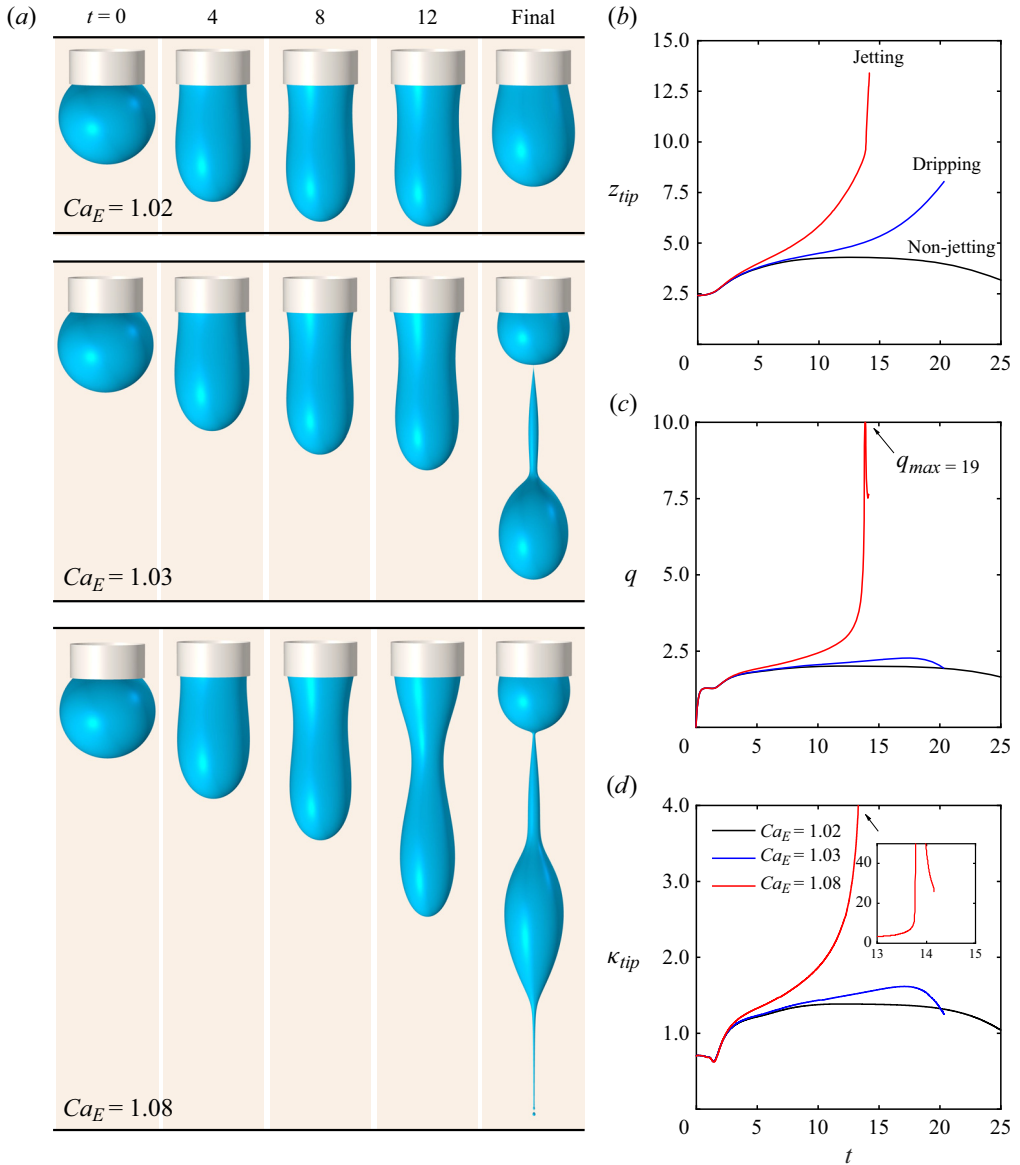
Figure 7. (*a*) Simulated images of time evolutions of the meniscus shapes in three regimes for $\theta_0 = 135°$. Effect of Ca_E on the temporal evolutions of physical quantities, (*b*) the axial location, (*c*) the charge density and (*d*) the curvature at the tip of the meniscus. Here, $\alpha = 10$.

process. Here the electric capillary number Ca_E is chosen to be 2.0 for all cases so that jetting can be ensured for all θ_0 ranging from 70° to 110°. It is observed that a liquid meniscus with a larger θ_0 will form a longer jet when pinch-off occurs. Compared with the limiting cases in figure 4, the cone angle decreases remarkably as the electric capillary number increases, resulting in the cone shape elongated to a larger extent. The subsequently emitted droplet adapts a teardrop shape and the thread connecting the jet and droplet becomes longer as θ_0 increases. Figure 8(*c*) shows that the size of the emitted droplet varies little with the opening half-angle θ_0, indicating that it does not depend on
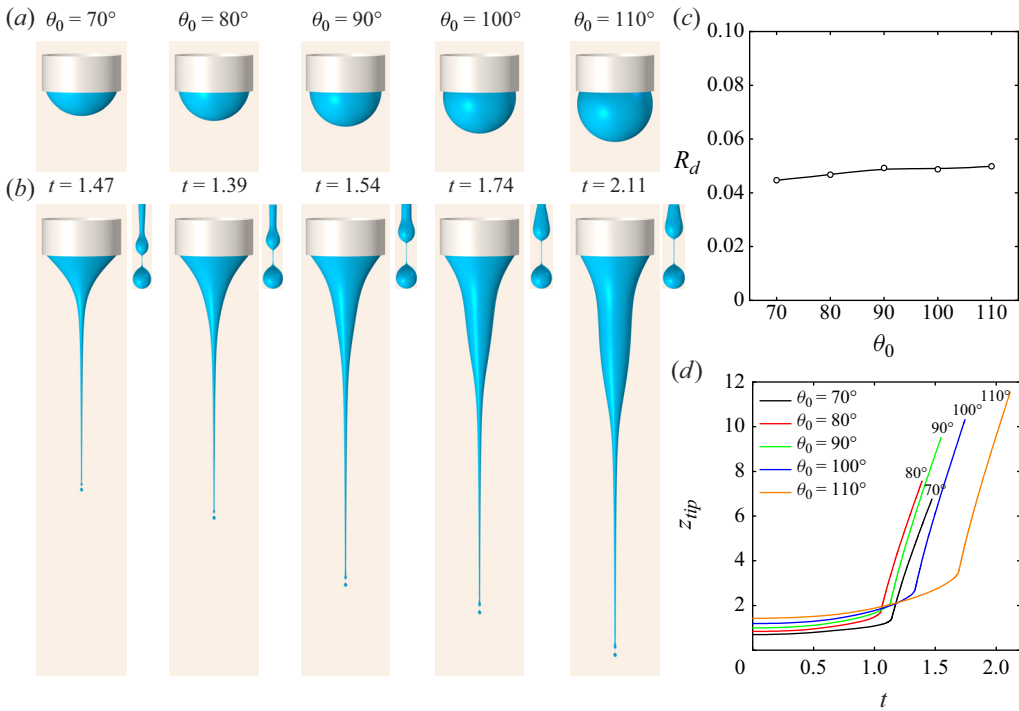
987 A38-14

Figure 8. Simulated meniscus shapes for different θ_0 at (a) $t = 0$ and (b) the incipience of pinch-off. Here, $Ca_E = 2.0$ and $\alpha = 10$ for all cases. In panel (b), the upper-right corner shows the magnified views of the tip-streaming jet's tip and the about-to-form droplet. Effect of θ_0 on the (c) size of the first emitted droplet and (d) temporal evolutions of the axial location at the tip of the meniscus.

the geometry of the liquid meniscus. This result yields the universality in the formation of a cone jet, which becomes valid when the radius of the jet is orders of magnitude smaller than the characteristic length scale. In this case, Gamero-Castaño & Magnani (2019) proposed that the characteristic only depends on the physical properties of the liquid meniscus, and is independent of the geometric and electrostatic variables (e.g. the dimensionless parameters θ_0 and Ca_E in this study). The present results therefore verify that the droplet emission from a liquid meniscus is expected to be a universal phenomenon.

Figure 8(d) shows the effect of θ_0 on the temporal evolutions of the axial location at the meniscus tip. It is seen that for $\theta_0 = 80°$, the value of pinch-off time is the smallest compared with that for the other θ_0. This is different from the results of limiting cases in figure 5(a) because the electric capillary number is kept the same in this case. The pinch-off time determines the frequency of the jet formation so that the underlying mechanism has to be answered. The reason for the tendency of pinch-off time can be found in figure 9, where the distributions of the electric field strength for different θ_0 are plotted at $t = 0$. Surprisingly, for the nozzle-to-plate configuration considered in our study, the local electric field at the meniscus tip just reaches its maximum when $\theta_0 = 80°$. The special distribution determines the magnitude of the initial electrical stresses imposed on the liquid interface. According to (2.7), the charge transport by Ohmic conduction depends on the local electric fields on both sides of the interface. Therefore, the higher electric field accelerates the transport of surface charge, which gives rise to earlier emission of the first droplet. This finding reveals the applicability of θ_0 as an index for evaluation of the time required for the tip streaming process and hence the frequency of droplet generation.
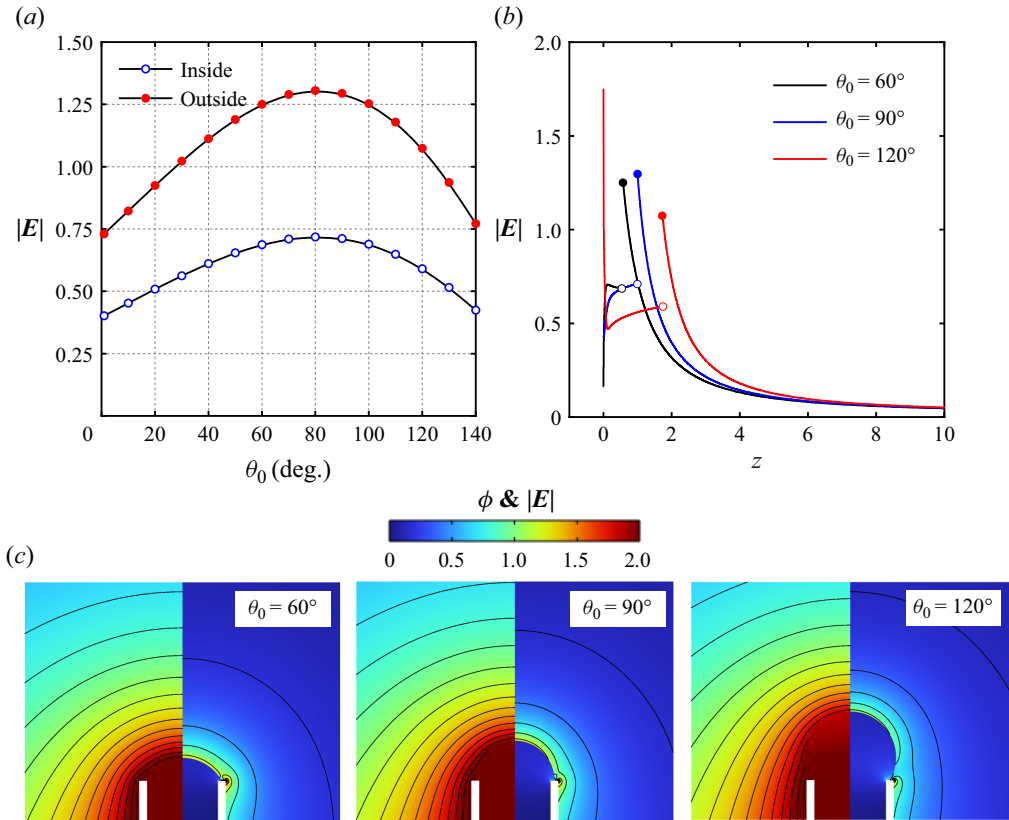
Figure 9. (*a*) Local electric fields at the tip of the meniscus for different θ_0. Here the blue and red points respectively represent the electric field strength inside and outside the drop. (*b*) Electric field strength along the meniscus interface and the symmetry axis as a function of the axial coordinate. Here, $z = 0$ denotes the triple contact point. (*c*) Distributions of the electric potential ϕ (left) and electric field strength $|E|$ (right) at $t = 0$ for $\theta_0 = 60°$, $90°$ and $120°$.

We then show the distribution of electric potential during the tip streaming process for the special case of $\theta_0 = 90°$. The contour in figure 10(*a*) indicates that the liquid seems to be nearly equipotential before the formation of tip streaming ($t = 1.1$). However, the equipotential assumption is no longer valid when tip streaming occurs at $t = 1.15$. The electric potential near the tip of the meniscus gradually reduces as the jet develops. When the first droplet is emitted at $t = 1.54$, the liquid again becomes an equipotential at the two ends of the thread.

Figure 10(*b*) shows the surface charge density as a function of the normalized arclength of the half-meniscus surface. The charge density at the meniscus tip is expected to increase quickly at $t = 1.15$ and decreases at $t = 1.45$ as a consequence of the jet development. In figure 10(*c*), we plot the normal and tangential electric stresses along the meniscus surface. The cone formation modifies the overall electric stress distribution. From the figure, the normal stress is always maximum at the tip, which is balanced by the capillary force caused by the sharp tip curvature. The tangential stress, which is nearly zero at $t = 1.1$, increases with time and leads to the tangential fluid flow. A high tangential stress region is created near the tip, which accelerates the flow towards the meniscus tip, thus developing the electrified jet. Both the normal and tangential electric stresses start to decrease with
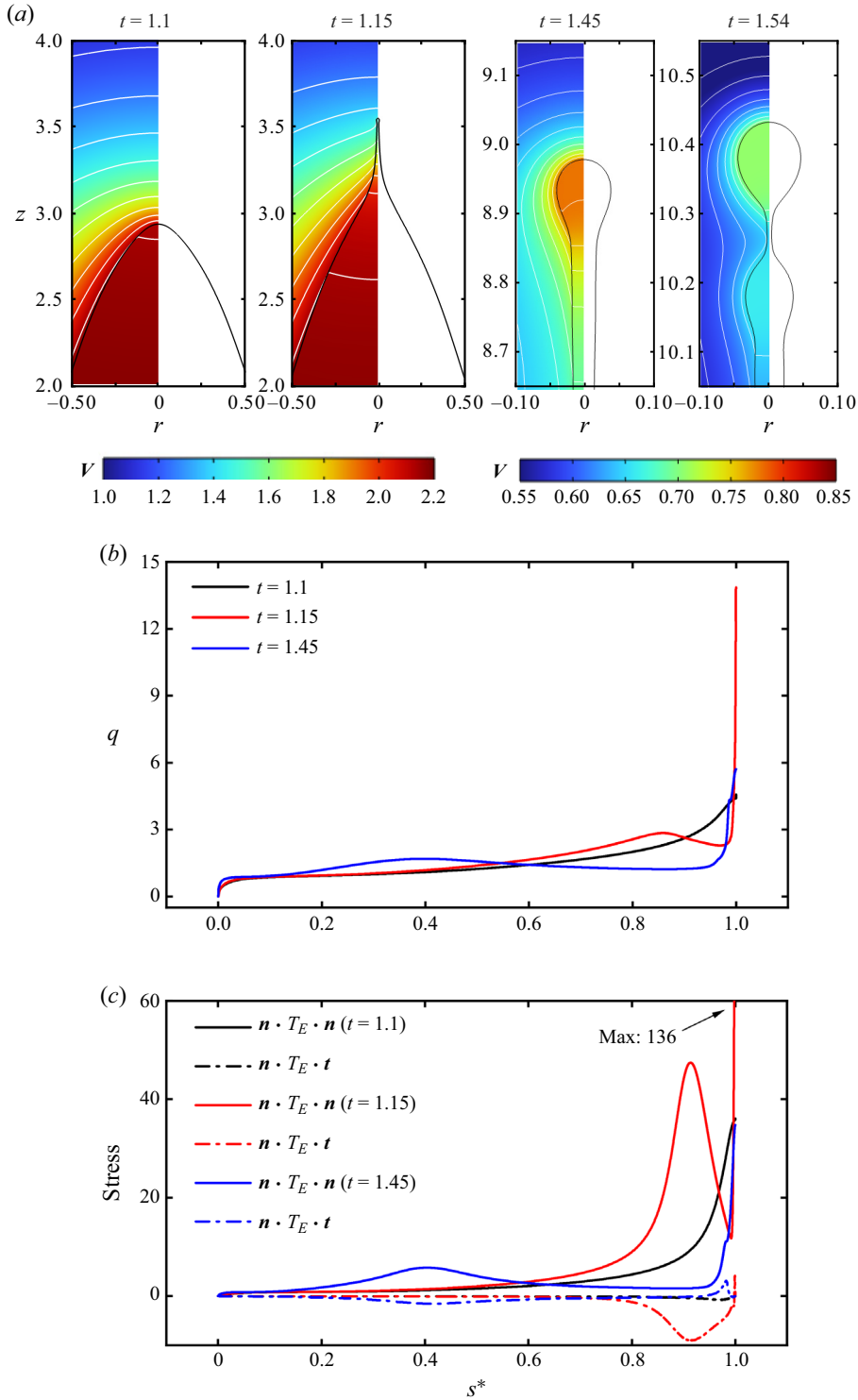
987 A38-16

Figure 10. (*a*) Distribution of electric potential at various times: $t = 1.1$, $t = 1.15$, $t = 1.45$ and $t = 1.54$ in the case of $\theta_0 = 90°$, $Ca_E = 2.0$ and $\alpha = 10$. Distributions of (*b*) charge density and (*c*) normal and tangential electric stresses on the half-meniscus surface as a function of the normalized arclength s^* at $t = 1.1$, $t = 1.15$ and $t = 1.45$. Here, $s^* = 0$ denotes the triple contact point.

the droplet emission. Moreover, the region with the maximum tangential stress gradually moves away from the tip of the meniscus as shown in the results at $t = 1.45$.

4.3. *Influence of electric capillary number on the tip streaming*

Further, to demonstrate the effect of electric field strength, the simulations were carried out for various Ca_E values. Figure 11(a–c) shows the meniscus shapes at the incipience of pinch-off for various values of Ca_E at $\theta_0 = 60°$, 90° and 120°, respectively. The jet length is obviously increased with the increase in Ca_E. Gawande *et al.* (2019) demonstrated that the jet length is governed by a balance of the tangential electric stress and the viscous stress. The formation of a tip-streaming jet requires a strong tangential electric stress. The increase in Ca_E leads to a growth of the tangential electric stress which accelerates the flow to the tip and results in the reduction of the pinch-off time, as shown in figure 11(d). Moreover, figure 11(e) shows that the size of the emitted droplets slightly increases with Ca_E, but are of the same order of magnitude, which further confirmed the role of universality in determining the formation of emitted droplets as discussed above.

4.4. *Influence of charge relaxation on the tip streaming*

Likewise, to demonstrate the effect of surface charge relaxation (i.e. the electric conductivity), we plot in figure 12(a–c) the meniscus shapes at the incipience of pinch-off for various values of α at $\theta_0 = 60°$, 90° and 120°, respectively. It is noted that the choice of different values of Ca_E for each θ_0 is determined to ensure the occurrence of jetting. The value of $\alpha = t_c/t_e$ represents the ratio of capillary time to the charge relaxation time. In the previous cases, we chose a constant value of $\alpha = 10$ so that the charge relaxation occurs as quickly as the fluid flow. However, as shown in figure 12, the tip-streaming shapes have been significantly altered when the charge relaxation parameter is varied from $\alpha = 0.01$ to 1000 with other parameters fixed.

We note that the jet length L_j increases with the increase in α and reaches its maximum at $\alpha = 10$, but decreases for higher values of α. This non-monotonic dependence is in agreement with the previous studies (Gawande *et al.* 2019). For a higher α, a long jet will form at the tip before the emission. Because the radius of the jet R_j is determined by the tip curvature of the electrified meniscus when the conical tip approaches the singularity, the liquid meniscus with a higher α will eject a thinner jet and thus a smaller droplet is emitted from the tip. Since the breakup of the jet is primarily induced by the Plateau–Rayleigh instability: $L_j > 2\pi R_j$, the jet length L_j therefore decreases with the increasing α. However, for lower α, the capillary force is dominant ($t_c/t_e \ll 1$) so that the capillary breakup occurs earlier than the formation of the jet. As a result, the thin jet has not formed completely for lower α and the jet length is still relatively short at the incipience of pinch-off.

To quantitatively describe the effect of charge relaxation, figure 13 shows the pinch-off time and the size of the emitted droplet as functions of α, respectively. A monotonic decrease in pinch-off time is observed with an increase in α. When α is increased by several orders of magnitude, the pinch-off time continuously decreases from ~100 to ~1. This can be attributed to the definition of α mentioned above. Tip streaming occurs only when the charge density at the tip reaches its limit so that the normal electric stress is strong enough to form the Taylor cone. The rate at which charge density rises primarily depends on the value of α. Therefore, an increase in α will promote the tip streaming process. Meanwhile, if α is high enough, its effect will become weaker since the transport
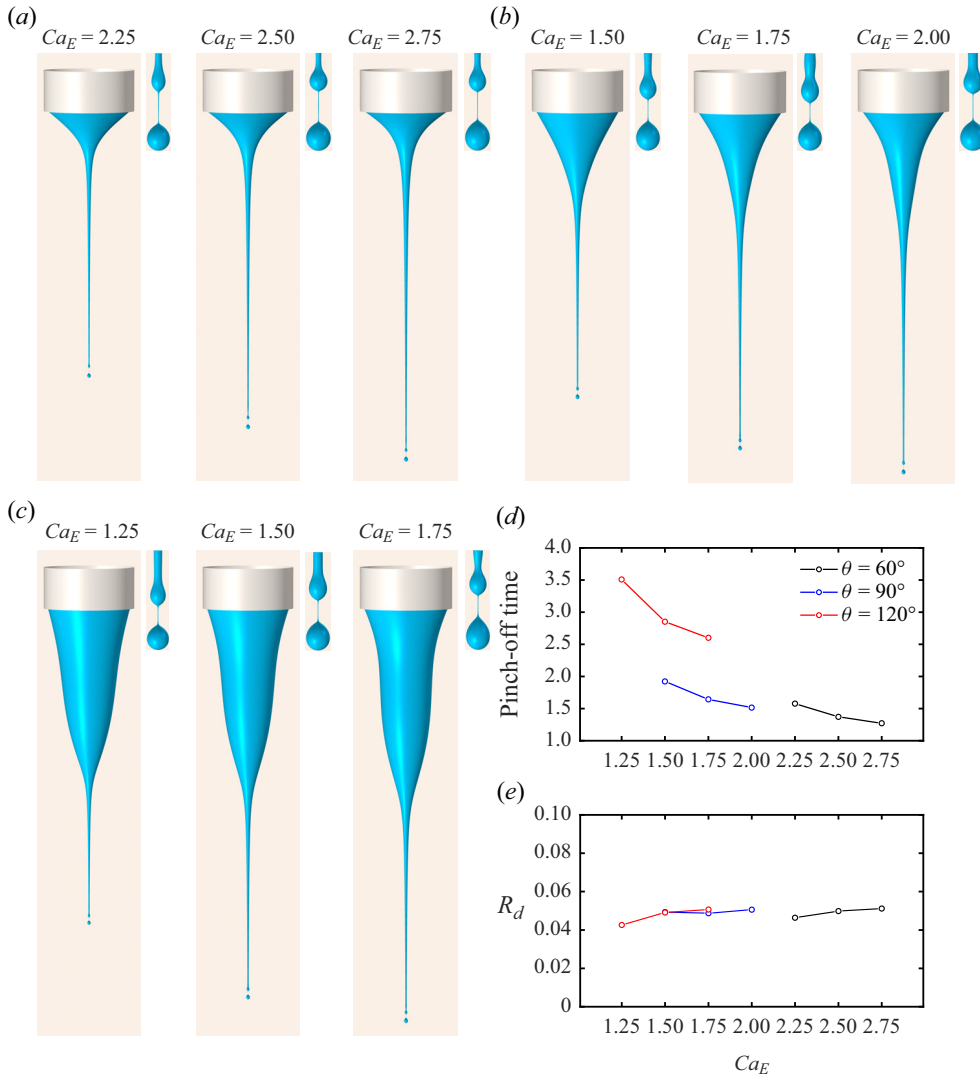
Figure 11. Simulated meniscus shapes at the incipience of pinch-off for different Ca_E at (*a*) $\theta_0 = 60°$, (*b*) $\theta_0 = 90°$ and (*c*) $\theta_0 = 120°$. The upper-right corner shows the magnified views of the tip-streaming jet's tip and the about-to-form droplet. Effect of Ca_E on the (*d*) pinch-off time and (*e*) size of the first emitted droplet. Here, $\alpha = 10$ for all cases.

of charge to the tip has already been as quick as the fluid flow. As shown in figure 13(*a*), the minimum values of the pinch-off time are approxiamtely 1.1, 1.4 and 3.0 for $\theta_0 = 60°$, $\theta_0 = 90°$ and $\theta_0 = 120°$, respectively.

Similarly, we observe a non-monotonic dependence of R_d on the charge relaxation α, as shown in figure 13(*b*). The accurate results show that the size of the first emitted droplet reaches its maximum at $\alpha \sim 5$. When $\alpha > 5$, the droplet size is found to decrease significantly to a small value, for example, the case with $\alpha = 1000$ produces a tiny droplet whose radius is only $\sim 0.1\%$ of the meniscus radius, e.g. 0.2 µm for a 200 µm nozzle. The variation of R_d in the limit of a high α is in accordance with the results of Collins *et al.* (2008). Moreover, a power-law relationship $R_d \sim \alpha^{-2/3}$ is observed, which is consistent
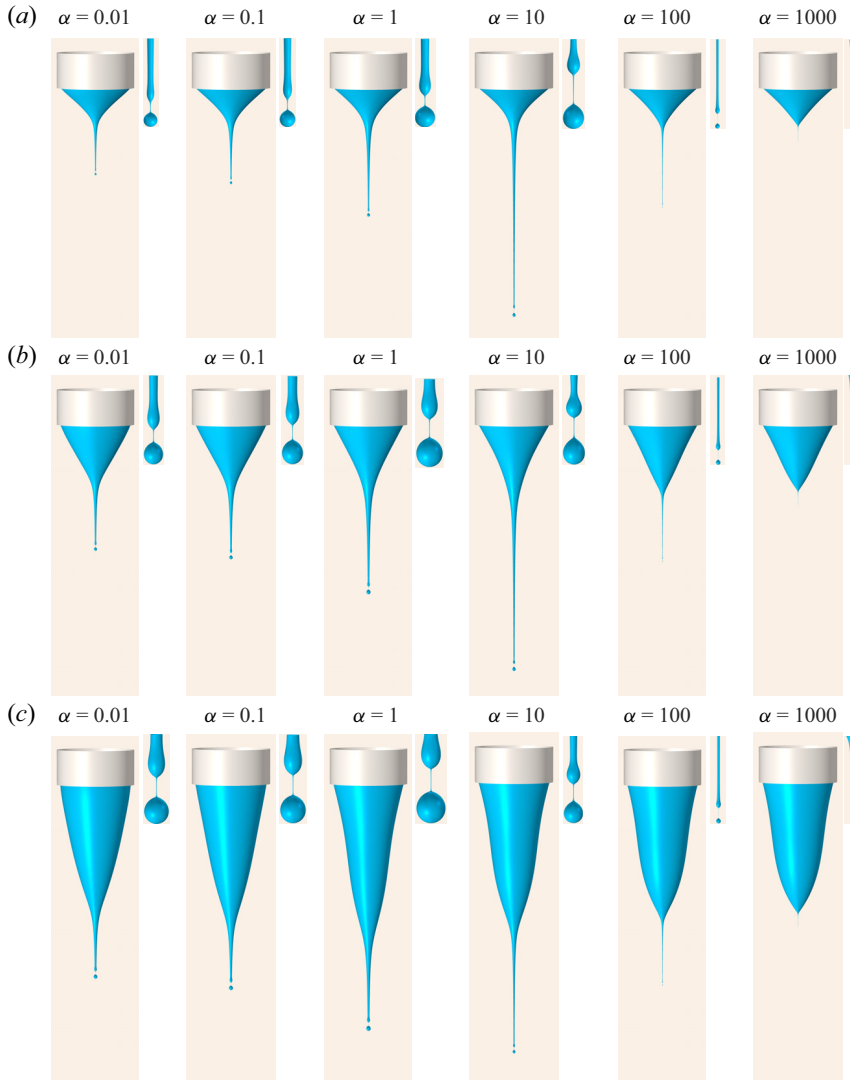
Figure 12. Simulated meniscus shapes at the incipience of pinch-off for different α at (*a*) $\theta_0 = 60°$ and $Ca_E = 2.25$, (*b*) $\theta_0 = 90°$ and $Ca_E = 1.5$, and (*c*) $\theta_0 = 120°$ and $Ca_E = 1.25$. The upper-right corner shows the magnified views of the tip-streaming jet's tip and the about-to-form droplet.

with the popular scaling law proposed by de la Mora & Loscertales (1994). They suggested that the size of the emitted droplet varies as $R_d \sim (\gamma/\rho)^{1/3} t_e^{2/3}$, namely, $R_d \sim \alpha^{-2/3}$ in the limit of large conductivities. However, at lower α, the size R_d is found to decrease slightly with decreasing α. The α dependence becomes weaker as the liquid approaches the dielectric limit ($\alpha \sim 0$).

To compare the jet shapes for different α, following Collins *et al.* (2013), we plot the simulated profiles of the jets at the incipiences of jet emission and pinch-off for α ranging from 0.01 to 1000, as shown in figure 14. Here, $\theta_0 = 90°$ and $Ca_E = 1.5$. When tip streaming occurs, the about-to-form jet shrinks as α is decreased to approach the dielectric limit ($\alpha \sim 0$) or increased to approach the perfectly conducting limit ($\alpha \sim \infty$), which is similar to that of the variation of the size of the emitted droplet. This result is beyond
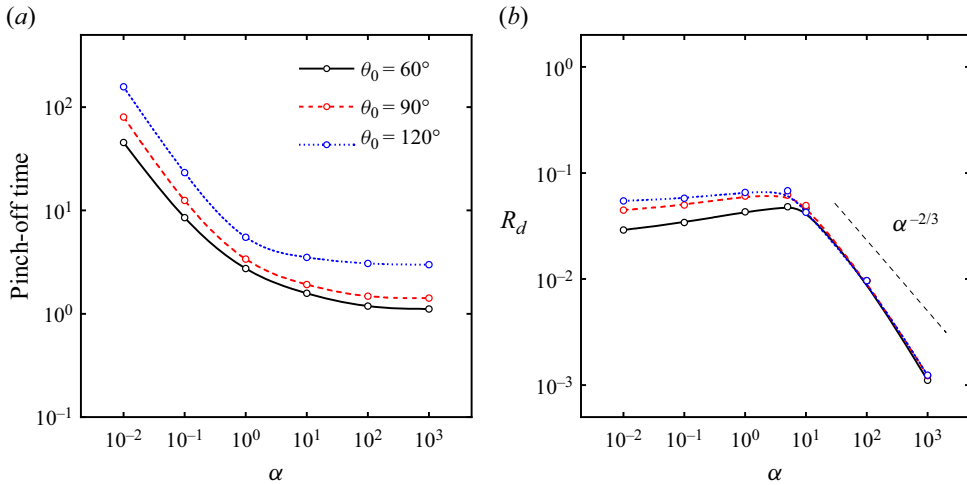
987 A38-20

Figure 13. Effect of α on the (*a*) pinch-off time and (*b*) size R_d of the first emitted droplet for $\theta_0 = 60°$ with $Ca_E = 2.25$, $\theta_0 = 90°$ with $Ca_E = 1.5$ and $\theta_0 = 120°$ with $Ca_E = 1.25$.

the previous studies. The slight decrease in droplet size in the dielectric limit has not been reported before. To identify the underlying mechanism, we plot in figure 15(*a*) the profiles of the tip-streaming jet's tip for $\alpha = 0.01$, $\alpha = 1$ and $\alpha = 100$, which represent respectively the cases of the dielectric, leaky-dielectric and conductor. It is observed that the jet radius is much smaller for $\alpha = 100$ than for $\alpha = 0.01$ and $\alpha = 1$. Obviously, this is due to the quick accumulation of surface charge since the jet behaves as a perfect conductor. However, when α decreases from 1 to 0.01, the jet shape is similar for the two cases, but the jet radius is slightly increased. From the shapes near the jet's tip, it is clear that the tip curvature is varied for all of the cases. According to the stress balance in (2.4), we thus show in figure 15(*b–d*) the distributions of the surface charge density, the normal electric stress and the tangential electric stress on the surface near the jet's tip. Figure 15(*b*) shows that the charge density q always reaches its maximum at the tip. However, the variation in q_{tip} (charge density at the tip) for different α shows a reversed trend as the jet radius, which results in a difference in the normal electric stresses on the surface, as shown in figure 15(*c*). The increase in the normal electric stress leads to a higher capillary pressure and thereby a higher tip curvature. This explains the non-monotonic dependence of R_d on α, as observed in simulations. However, another question must be answered: Why is the charge density at the tip for $\alpha = 1$ smaller than that for $\alpha = 0.01$? Actually, from the charge transport equation (2.7), for low α values, surface charge convection becomes dominant in charge transport compared with conduction (Sengupta, Walker & Khair 2017; Nie *et al.* 2021*b*). As α is reduced to 0.01, the significance of the convection at the tip exceeds the conduction and leads to a slight increase in charge density compared with the case where $\alpha = 1$. Moreover, figure 15(*d*) shows the distribution of the tangential electric stress that accelerates the axial flow of the jet, which also indicates the importance of flow-induced charge convection in charge transport. From the discussion above, we propose that to obtain a larger size of the first emitted droplet, the fluid conductivity should be controlled within a specific range.
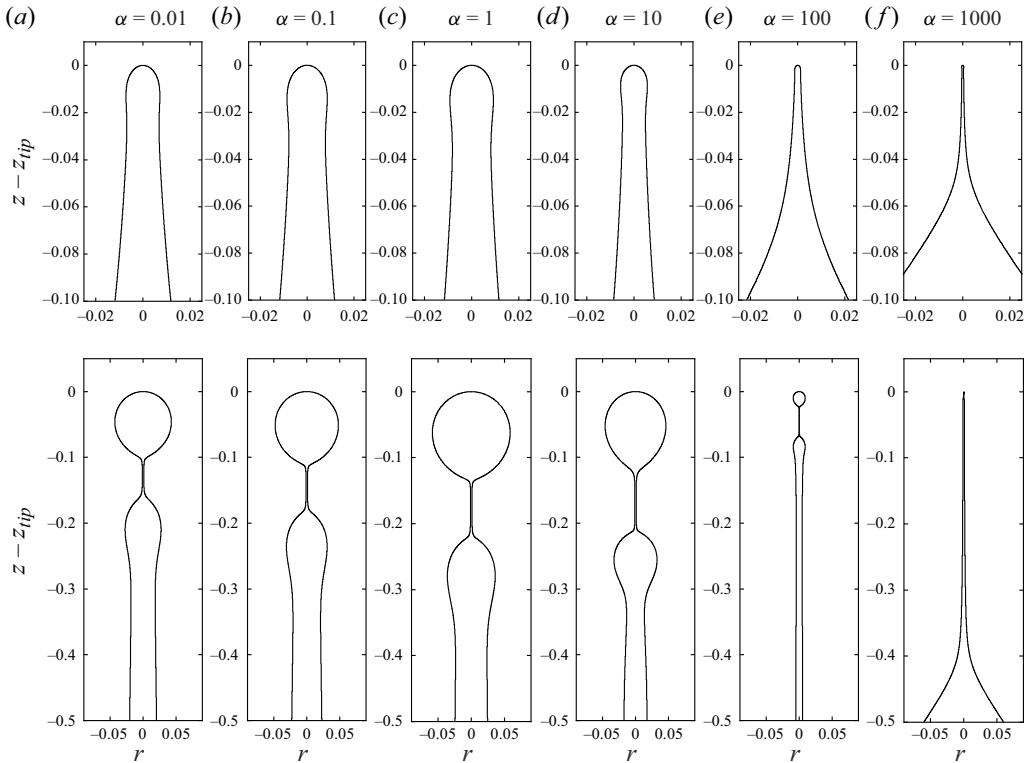
Figure 14. Profiles of the tip-streaming jet's tip and the about-to-form droplet at the incipiences of jet emission (upper) and pinch-off (lower) for α values of (a) 0.01, (b) 0.1, (c) 1, (d) 10, (e) 100 and (f) 1000. Here, $\theta_0 = 90°$ and $Ca_E = 1.5$.

5. Conclusion

In the present study, we have numerically investigated the first emission of a charged droplet from an electrified meniscus hanging at the nozzle tip. The non-uniform distribution of electric field is solved for a nozzle-to-plate configuration and coupled to the Navier–Stokes equations. The numerical model has been validated against the experimental observation from Ferrera *et al.* (2013). This model enables us to simulate the tip streaming process of a liquid meniscus hanging at the nozzle tip when subjected to an electric field, with a focus on the pinch-off time, jet length and size of the first emitted droplet. We determined the critical electric capillary number for the occurrence of tip streaming as a function of the initial liquid volume. Three distinct regimes, including non-jetting, jetting and dripping, are identified in a phase diagram. We demonstrate that the key factor that determines the difference between these three regimes is the speed at which the tip charge density rises.

Next, we investigate the influences of the initial liquid volume, electric field strength and electrical conductivity of the liquid on the emission of the charged droplet. We find that the pinch-off time reaches its maximum for $\theta_0 = 80°$, where the opening half-angle θ_0 represents the initial liquid volume. We demonstrate that this is attributed to the special distribution of electric field in a nozzle-to-plate configuration. Then we analyse the roles of the normal and tangential electric stresses during the tip streaming process. The increase in the electric field strength leads to a growth of the tangential electric
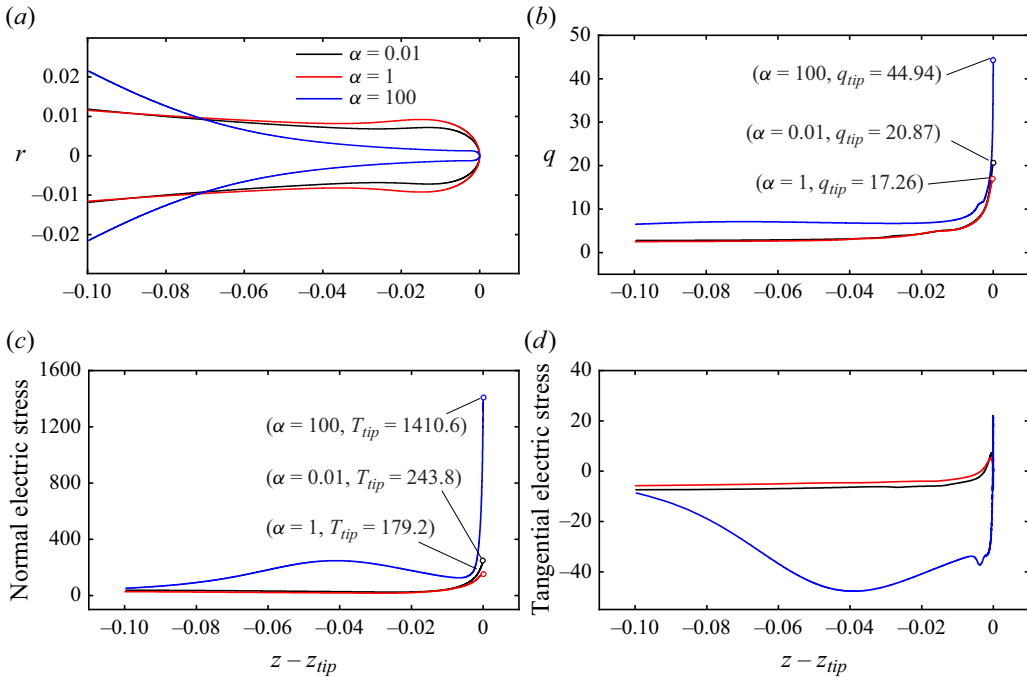
987 A38-22

Figure 15. (*a*) Profiles of the tip-streaming jet's tip at the incipiences of jet emission for α values of 0.01 (black), 1 (red) and 100 (blue). Here, $\theta_0 = 90°$ and $Ca_E = 1.5$. Distributions of (*b*) surface charge density, (*c*) normal electric stress and (*d*) tangential electric stress on the surface near the jet's tip at the incipiences of emission. In panels (*b*) and (*c*), the values at the tips have been marked.

stress which accelerates the flow to the tip and results in the reduction of the pinch-off time. Finally, we systematically discuss the effect of surface charge relaxation α (i.e. the electric conductivity) on the size R_d of the first emitted droplet. We find a particularly non-monotonic dependence of R_d on α. The size of the first emitted droplet reaches its maximum at $\alpha \sim 5$. When $\alpha > 5$, the droplet size is found to decrease significantly to a small value. However, at lower α, the size R_d is found to decrease slightly with decreasing α as the liquid approaches the dielectric limit. The non-monotonic dependence is explained by the increasing role of surface charge convection in charge transport compared with conduction. These results can serve as a guide for the working conditions of EHD printing devices, for instance, by selecting the critical voltage for given fluid properties and geometry of the nozzle and collector electrodes to obtain a jetting mode.

Funding. This work was supported by the National Key Research and Development Program of China (2018YFA0703203) and the National Natural Science Foundation of China (grant no. 52276064).

Declaration of interests. The authors report no conflict of interest.

Author ORCIDs.

 Hao Chen https://orcid.org/0000-0002-6073-5338;

 Guozhen Wang https://orcid.org/0000-0003-1793-8508;

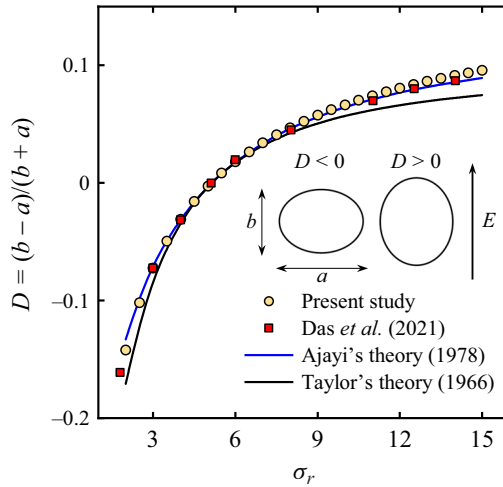 Haisheng Fang https://orcid.org/0000-0002-4436-803X.

Figure 16. Deformation D as a function of the conductivity ratio σ_r. Here, $Ca_E = 0.18$, $\varepsilon_r = 10$, $\mu_r = 1$ and $Oh = 3.16$. The circle symbols correspond to our simulations and the square symbols correspond to the simulations of Das *et al.* (2021). The black and blue lines respectively represent the analytical solutions of Taylor (1966) and Ajayi (1978).

Appendix A. Validation of the electrohydrodynamic model

We validate the electrohydrodynamic model in this study by considering a realistic problem. A liquid droplet suspended in a second liquid domain is simulated when subjected to a uniform electric field. The droplet will be deformed under the electric force and eventually reach a steady state. The deformation parameter D of the droplet is defined as $D = (b - a)/(b + a)$, where b and a are the lengths of the deformed droplet in the direction parallel and vertical to the electric field, respectively. Taylor (1966) analytically provided a relationship between the deformation D and the electric capillary number, as

$$D = \frac{9}{16} \frac{Ca_E}{(2 + \sigma_r)} \left[1 + \sigma_r^2 - 2\varepsilon_r + \frac{3}{5}(\sigma_r - \varepsilon_r)\frac{2 + 3\mu_r}{1 + \mu_r} \right], \tag{A1}$$

where σ_r, ε_r and μ_r denote the conductivity, permittivity and viscosity ratios of the droplet to the surrounding medium. We employ the same setting as Das, Dalal & Tomar (2021), where $Ca_E = 0.18$, $\varepsilon_r = 10$, $\mu_r = 1$ and $Oh = 3.16$, so that the deformation D is only dependent of the conductivity ratio σ_r. Figure 16 shows the comparison between our simulation results and previous studies. We observe that there is a good agreement between our model and the theory, especially compared with Ajayi's second-order theory (Ajayi 1978). The numerical model is therefore validated in modelling the electrohydrodynamic problem.

REFERENCES

AJAYI, O.O. 1978 A note on Taylor's electrohydrodynamic theory. *Proc. R. Soc. Lond.* A*: Math. Phys. Sci.* **364**, 499–507.
ANTHONY, C.R., *et al*. 2023 Sharp interface methods for simulation and analysis of free surface flows with singularities: breakup and coalescence. *Annu. Rev. Fluid Mech.* **55**, 707–747.
BASARAN, O.A., GAO, H. & BHAT, P.P. 2013 Nonstandard inkjets. *Annu. Rev. Fluid Mech.* **45**, 85–113.
BEROZ, J., HART, A.J. & BUSH, J.W.M. 2019 Stability limit of electrified droplets. *Phys. Rev. Lett.* **122**, 244501.

CHEN, H., CHEN, W., YIN, Z. & FANG, H. 2023 Electrohydrodynamic-induced partial coalescence between a droplet and a liquid–air interface. *J. Fluid Mech.* **963**, A39.

CISQUELLA-SERRA, A., MAGNANI, M., GUAL-MOSEGUI, Á, HOLMBERG, S., MADOU, M. & GAMERO-CASTAÑO, M. 2019 Study of the electrostatic jet initiation in near-field electrospinning. *J. Colloid Interface Sci.* **543**, 106–113.

CLOUPEAU, M. & PRUNET-FOCH, B. 1990 Electrostatic spraying of liquids: main functioning modes. *J. Electrostat.* **25**, 165–184.

CLOUPEAU, M. & PRUNET-FOCH, B. 1994 Electrohydrodynamic spraying functioning modes: a critical review. *J. Aerosol Sci.* **25**, 1021–1036.

COLLINS, R.T., JONES, J.J., HARRIS, M.T. & BASARAN, O.A. 2008 Electrohydrodynamic tip streaming and emission of charged drops from liquid cones. *Nat. Phys.* **4**, 149–154.

COLLINS, R.T., SAMBATH, K., HARRIS, M.T. & BASARAN, O.A. 2013 Universal scaling laws for the disintegration of electrified drops. *Proc. Natl Acad. Sci. USA* **110**, 4905–4910.

DAS, S.K., DALAL, A. & TOMAR, G. 2021 Electrohydrodynamic-induced interactions between droplets. *J. Fluid Mech.* **915**, A88.

FENN, J.B., MANN, M., MENG, C.K., WONG, S.F. & WHITEHOUSE, C.M. 1989 Electrospray ionization for mass spectrometry of large biomolecules. *Science* **246** (4926), 64–71.

FERRERA, C., LÓPEZ-HERRERA, J.M., HERRADA, M.A., MONTANERO, J.M. & ACERO, A.J. 2013 Dynamical behavior of electrified pendant drops. *Phys. Fluids* **25**, 012104.

GALLUD, X. & LOZANO, P.C. 2022 The emission properties, structure and stability of ionic liquid menisci undergoing electrically assisted ion evaporation. *J. Fluid Mech.* **933**, A43.

GAMERO-CASTAÑO, M. & MAGNANI, M. 2018 Numerical simulation of electrospraying in the cone-jet mode. *J. Fluid Mech.* **859**, 247–267.

GAMERO-CASTAÑO, M. & MAGNANI, M. 2019 The minimum flow rate of electrosprays in the cone-jet mode. *J. Fluid Mech.* **876**, 553–572.

GAÑÁN-CALVO, A.M., LASHERAS, J.C., DÁVILA, J. & BARRERO, A. 1994 The electrostatic spray emitted from an electrified conical meniscus. *J. Aerosol Sci.* **25**, 1121–1142.

GAÑÁN-CALVO, A.M., LÓPEZ-HERRERA, J.M., HERRADA, M.A., RAMOS, A. & MONTANERO, J.M. 2018 Review on the physics of electrospray: from electrokinetics to the operating conditions of single and coaxial Taylor cone-jets, and AC electrospray. *J. Aerosol Sci.* **125**, 32–56.

GAÑÁN-CALVO, A.M., LÓPEZ-HERRERA, J.M., REBOLLO-MUÑOZ, N. & MONTANERO, J.M. 2016 The onset of electrospray: the universal scaling laws of the first ejection. *Sci. Rep.* **6**, 1–9.

GAWANDE, N., MAYYA, Y.S. & THAOKAR, R. 2019 Jet and progeny formation in the Rayleigh breakup of a charged viscous drop. *J. Fluid Mech.* **884**, A31.

GUAN, Y., WU, S., WANG, M., TIAN, Y., YU, C., LAI, W. & HUANG, Y. 2022 Numerical investigation of high-frequency pulsating electrohydrodynamic jet at low electric Bond numbers. *Phys. Fluids* **34**, 012001.

HARRIS, M.T. & BASARAN, O.A. 1993 Capillary electrohydrostatics of conducting drops hanging from a nozzle in an electric field. *J. Colloid Interface Sci.* **161**, 389–413.

HIJANO, A.J., LOSCERTALES, I.G. & HIGUERA, F.J. 2021 Modelling the electric microdripping from a needle. *J. Fluid Mech.* **920**, A47.

HIJANO, A.J., LOSCERTALES, I.G., IBÁÑEZ, S.E. & HIGUERA, F.J. 2015 Periodic emission of droplets from an oscillating electrified meniscus of a low-viscosity, highly conductive liquid. *Phys. Rev.* E **91**, 1–12.

ISMAIL, A.S., YAO, J., XIA, H.H. & STARK, J.P.W. 2018 Breakup length of electrified liquid jets: scaling laws and applications. *Phys. Rev. Appl.* **10**, 064010.

JAWOREK, A. & KRUPA, A. 1999 Classification of the modes of EHD spraying. *J. Aerosol Sci.* **30**, 873–893.

KONG, Q., YANG, S., WANG, Q., WANG, Z., DONG, Q., & WANG, J. 2022 Dynamics of electrified jets in electrohydrodynamic atomization. *Case Stud. Therm. Engng* **29**, 101725.

LEE, A., JIN, H., DANG, H.W., CHOI, K.H. & AHN, K.H. 2013 Optimization of experimental parameters to determine the jetting regimes in electrohydrodynamic printing. *Langmuir* **29**, 13630–13639.

LOHSE, D. 2022 Fundamental fluid dynamics challenges in inkjet printing. *Annu. Rev. Fluid Mech.* **54**, 349–382.

LÓPEZ-HERRERA, J.M., HERRADA, M.A. & GAÑÁN-CALVO, A.M. 2023 Electrokinetic modelling of cone-jet electrosprays. *J. Fluid Mech.* **964**, A19.

MARGINEAN, I., NEMES, P. & VERTES, A. 2006 Order-chaos-order transitions in electrosprays: the electrified dripping faucet. *Phys. Rev. Lett.* **97**, 1–4.

MELCHER, J.R. & TAYLOR, G.I. 1969 Electrohydrodynamics: a review of the role of interfacial shear stresses. *Annu. Rev. Fluid Mech.* **1**, 111–146.

MONTANERO, J.M. & GAÑÁN-CALVO, A.M. 2020 Dripping, jetting and tip streaming. *Rep. Prog. Phys.* **83**, 097001.

DE LA MORA, J.F. & LOSCERTALES, I.G. 1994 The current emitted by highly conducting Taylor cones. *J. Fluid Mech.* **260**, 155–184.

NIE, Q., LI, F., MA, Q., FANG, H. & YIN, Z. 2021*b* Effects of charge relaxation on the electrohydrodynamic breakup of leaky-dielectric jets. *J. Fluid Mech.* **925**, 1–29.

NIE, Q., MA, Q., YANG, W., PAN, X., LIU, Z., FANG, H. & YIN, Z. 2021*a* Designing working diagrams for electrohydrodynamic printing. *Chem. Engng Sci.* **240**, 116661.

NOTZ, P.K. & BASARAN, O.A. 1999 Dynamics of drop formation in an electric field. *J. Colloid Interface Sci.* **213**, 218–237.

PARK, J.U., *et al.* 2007 High-resolution electrohydrodynamic jet printing. *Nat. Mater.* **6**, 782–789.

RUBIO, M., RODRÍGUEZ-DÍAZ, P., LÓPEZ-HERRERA, J.M., HERRADA, M.A., GAÑÁN-CALVO, A.M. & MONTANERO, J.M. 2023 The role of charge relaxation in electrified tip streaming. *Phys. Fluids* **35**, 017131.

RUBIO, M., SADEK, S.H., GAÑÁN-CALVO, A.M. & MONTANERO, J.M. 2021 Diameter and charge of the first droplet emitted in electrospray. *Phys. Fluids* **33**, 032002.

SAVILLE, D.A. 1997 Electrohydrodynamics: the Taylor-Melcher leaky dielectric model. *Annu. Rev. Fluid Mech.* **29**, 27–64.

SENGUPTA, R., WALKER, L.M. & KHAIR, A.S. 2017 The role of surface charge convection in the electrohydrodynamics and breakup of prolate drops. *J. Fluid Mech.* **833**, 29–53.

TAYLOR, G. 1964 Disintegration of water drops in an electric field. *Proc. R. Soc. Lond.* A*: Math. Phys. Sci.* **280**, 383–397.

TAYLOR, G. 1966 Studies in electrohydrodynamics. I. The circulation produced in a drop by an electric field. *Proc. R. Soc. Lond.* A*: Math. Phys. Sci.* **291**, 159–166.

VERDOOLD, S., AGOSTINHO, L.L.F., YURTERI, C.U. & MARIJNISSEN, J.C.M. 2014 A generic electrospray classification. *J. Aerosol Sci.* **67**, 87–103.

VLAHOVSKA, P.M. 2019 Electrohydrodynamics of drops and vesicles. *Annu. Rev. Fluid Mech.* **51**, 305–330.

WAGONER, B.W., VLAHOVSKA, P.M., HARRIS, M.T. & BASARAN, O.A. 2021 Electrohydrodynamics of lenticular drops and equatorial streaming. *J. Fluid Mech.* **925**, A36.

WENDORFF, J.H., AGARWAL, S. & GREINER, A. 2012 *Electrospinning*. Wiley.

ZELENY, J. 1917 Instability of electrified liquid surfaces. *Phys. Rev.* **10**, 1–6.

ZHONG, S., LU, Y., YANG, Y., ZHAO, Y., YANG, Y. & PENG, Y. 2023 Numerical investigation of the effect of operating parameters on droplet ejection in a double ring electrohydrodynamic printing device. *J. Electrostat.* **122**, 103795.